

# Research on In-plane Thermoelectric Elements Using the Spin Seebeck Effect

Tatsuhiko NOZUE<sup>\*1</sup>, Tadashi MORITA<sup>\*1</sup> and Hirohiko MURAKAMI<sup>\*1</sup>

<sup>\*1</sup> Future Technology Research Laboratory, ULVAC, Inc., 5-9-6 Tohkohdai, Tsukuba, Ibaraki 300-2635 Japan

We have investigated the thermoelectric elements using the spin Seebeck effect (SSE), in order to develop the novel thermoelectric device. The multilayered SSE elements of  $Y_3Fe_5O_{12}$  (YIG) and Pt,  $[YIG/Pt]_n$ , were fabricated by sputtering. The sample of  $n = 2$  had the SSE coefficient 2 times as large as that of  $n=1$ . However, the SSE of  $n = 3$  sample was almost equal to that of  $n = 2$ . This enhancement of SSE is considered to be contributed by the spin current enhanced in the multilayer  $[YIG/Pt]_n$ .

## 1. Introduction

### 1.1 Background

Information terminals have been getting smaller in recent years, going from PCs to smart phones and then evolving into miniature devices such as smart watches. However, miniaturization limits battery size. Therefore, devices are expected to become equipped with so-called energy-harvesting capabilities. Among the possible energy-harvesting techniques, a power generator that utilizes body heat is suitable for such mobile devices. Therefore, research and development efforts to make thermoelectric devices thin and flexible are advancing. We have investigated the basic principle of the spin Seebeck effect (SSE) as one of the new thermoelectric principles utilizing magnetism, as well as ways to improve its thermoelectric efficiency; we report the results here<sup>1), 2)</sup>.

In recent years, the Spin Hall Effect (SHE) and the Inverse Spin Hall Effect (ISHE) induced by spin-orbit interaction (SOI) have been attracting much attention. SHE and ISHE are physical phenomena caused by the transport of magnetic polarization by means of "spin current," which is not accompanied by charge transfer. In the conventional Hall effect, when an electric current is applied to a metal or semiconductor in a magnetic field, the Lorentz Force creates an electric field in the direction perpendicular to the magnetic field and the electric current. In SHE, however, SOI produces forces in an opposite direction depending on whether the spin is up or down. Consequently, when an electric current is applied to a metal in a magnetic field, the deviation from the equilibrium of the spin (spin accumulation) occurs in the direction perpendicular to the magnetic field and the electric current. ISHE is the inverse phenomenon from SHE. Thus, when a spin current is applied to a metal in a magnetic field, the charge accumulates in the direction perpendicular to both the magnetic field and the spin current, creating an electric field. The spin current has only a micro diffusion length. However, thanks to advances in research on magnetic properties in micro areas, the existence of spin currents has been proven through SHE and ISHE, and ISHE has been established as the methodology for searching for a spin current.

The spin Seebeck effect (SSE) is a phenomenon in which an electric current occurs when a temperature difference exists in the stacking direction of a bi-layer consisting of a magnetized ferromagnetic material and a nonmagnetic

metal. The electric current thus generated is proportional to the temperature difference and flows perpendicular to both the orientation of the magnetization inside the nonmagnetic metal and the direction of the temperature difference. The spin current generated by the concentration distribution of the spin waves (magnons) excited by the heat along the temperature gradient inside the ferromagnetic material causes an accumulation in the spin at the interface between the ferromagnetic material and the nonmagnetic metal, thus causing a spin current inside the nonmagnetic metal, as well. From the spin current inside the nonmagnetic metal, an electric current occurs according to ISHE. As mentioned above, SSE is understood to be a complex phenomenon. In the ferromagnetic insulator, it can be presumed that pure spin currents are carried by magnons, because there are no electrons carrying the heat and the spin flow.

In SSE, unlike in the conventional Seebeck effect, the direction of the temperature difference is perpendicular to the direction of the electrical current. A commercially available Seebeck element is formed using a  $\Pi$  shape in which p- and n-type devices are alternately bonded. This results in a large element area, which increases the manufacturing costs. In contrast, with SSE, an equivalent amount of power can be generated by simply stacking a ferromagnetic film and a nonmagnetic film, thus reducing costs by fabricating a simple structure. SSE elements in which coating or spraying was used to fabricate a ferromagnetic material have actually been reported<sup>1)</sup>. Moreover, because the heat carrier (magnons) differs from the charge carrier (electrons), no limitations are posed by the Wiedemann-Franz law, which would become a problem in the conventional Seebeck effect. Theoretically, it is expected that an efficiency level exceeding that achievable with the conventional Seebeck effect can be obtained. However, in actual elements, power generation efficiency has been achieved of only around 1/10,000 that of thermoelectric elements such as Bi-Te. There are many factors that reduce the power generation efficiency, including the percentage of the heat carried by the spin currents, the efficiency at which spin currents are injected from the ferromagnetic material into the nonmagnetic metal, and the conversion efficiency from the spin currents to electrical current. In other words, many issues must be resolved before SSE elements can be used realistically as thermoelectric elements.

Because SSE in a Pt/YIG junction was observed in 2010, this specimen structure has been used in many research projects as the prototype for a thermal spin current generation element that uses an insulator. Since the atomic nuclei of the 5d electron system have a large charge, the SOI tends

<sup>\*1</sup> Future Technology Research Laboratory, ULVAC, Inc., 5-9-6 Tokodai, Tsukuba, Ibaraki, 300-2635 Japan

to be large. In particular, because Pt has a large SHE due to its band structure, it has become an essential material in spin current research.

## 1.2 Purpose

We had expected that increasing the thermoelectric output from the SSE elements would simply be a matter of increasing the thickness of the nonmagnetic metal layers, which we assumed would have a multiplying effect on the electric current. However, because Pt has a large ISHE, the spin current will be propagated to a distance of only 5 nm at the most. Even if the film is thicker than this propagation distance (spin current diffusion length), SSE will not increase. Therefore, creating a multilayered structure consisting of ferromagnetic layers and nonmagnetic layers becomes the key for resolving the issue.

The thermoelectric properties of  $\text{MgO}/[\text{Fe}_3\text{O}_4/\text{Pt}]_n$  from  $n = 1$  to 6 were investigated, in which bilayers of magnetite ( $\text{Fe}_3\text{O}_4$ ) and Pt are stacked  $n$  times, and increases in the sSE voltage of up to 5.5 times relative to when  $n = 1$  have been reported<sup>3)</sup>. These large voltages are considered to be the contribution to SSE made by the large spin currents within the  $[\text{Fe}_3\text{O}_4/\text{Pt}]_n$  multilayered structure. Figure 1 shows the distribution of spin currents in the film thickness direction in a single-layer film and a 4-layer film, as calculated in Reference 3. Spin currents increase up to around the spin current diffusion length. Therefore, if the film thickness of the  $\text{Fe}_3\text{O}_4$  film is thinner than the diffusion length, the maximum value of the spin current increases as the number of layers increases. On the other hand, because the spin currents

are zero at both ends of  $[\text{Fe}_3\text{O}_4/\text{Pt}]_n$ , they become small on the Pt that is on the outermost surface, and the SSE voltage is also small. In a multilayered structure such as  $[\text{Fe}_3\text{O}_4/\text{Pt}]_4$ , there are Pt layers located in a position away from both ends, and therefore a large spin current is injected into the Pt, as indicated by the arrow in the figure. Because of a substantial increase in the film thickness and the injection of spin current into the Pt, which is far away from the end faces, spin currents that are greater by several times are converted into electrical current through the inverse spin Hall effect. In this multilayered film, because conductance through the Pt layers increases according to the number of Pt layers, the output increases by more than 100 times. If a multilayered film of  $[\text{YIG}/\text{Pt}]_n$  can be fabricated using YIG, which has a longer diffusion length than  $\text{Fe}_3\text{O}_4$  (which has a diffusion length of around 30 nm), even greater boosting of the SSE voltage can be expected.

In our research, we fabricated a high-quality YIG film with sputtering in order to validate the effects of multilayered films, and we examined (1) dependence of YIG/Pt on SSE film thickness, (2) dependence of multilayered  $[\text{YIG}/\text{Pt}]_n$  ( $n = 1-3$ ) on the number of SSE layers, and (3) an SSE element with a sandwich structure of Pt/YIG/Pt.

## 2. Experiment method

### 2.1 Film deposition method

$\text{Y}_3\text{Fe}_5\text{O}_{12}$  (YIG) is an oxide with a garnet structure and is a ferrimagnetic insulator with  $T_c = 286^\circ\text{C}$ . Its lattice constant has been reported to be 1.2376 nm, which is extremely close to the lattice constant of the nonmagnetic insulator  $\text{Gd}_3\text{Ga}_5\text{O}_{12}$  (GGG), which is 1.2383 nm. Because the lattice mismatch is only 0.06%, we can obtain a high-quality YIG film by depositing it on a GGG substrate. An oxide with a garnet structure can generally be written as  $\text{C}_3\text{A}_2\text{D}_3\text{O}_{12}$ . This is a large cubic unit cell containing eight units, and in YIG, C becomes  $\text{Y}^{3+}$ , A becomes  $\text{Fe}^{3+}$ , and D becomes  $\text{Fe}^{3+}$ .  $\text{Fe}^{3+}$  occupies two different sites, both of which are positioned within the polyhedron formed by  $\text{O}^{2-}$ . Site A is an octahedron and site D is a tetrahedron, and they are linked to each other via O. The localized spin in site A is oriented in the opposite direction from that in site D, and YIG has a net amount of magnetization per unit cell ( $5 \mu_B$ ) equal to that of a single  $\text{Fe}^{3+}$ . The magnetization of bulk YIG has been reported to be  $140 \text{ emu cm}^{-3}$  at room temperature.

The experiments in this study were performed using the facility of Saitoh Laboratory at the Advanced Institute for Materials Research (AIMR), Tohoku University. The sputtering system, QAM-4-STs, made by ULVAC Kyushu Corporation, was used to deposit YIG and Pt films. This system consists of  $4 \times 2$  chambers + transfer chamber + load lock, and the background pressure in the deposition chamber is above  $10^{-6}$  Pa. Transfer, heating, and film deposition are carried out automatically according to deposition recipes. For the substrate for film deposition, we used single-crystalline GGG substrates with (110) orientation, a size of  $10 \times 10 \times 0.5$  mm thick, and one side polished. The film deposition conditions were as follows:

Pt: Ar 15 sccm, DC20 W, 260 s,

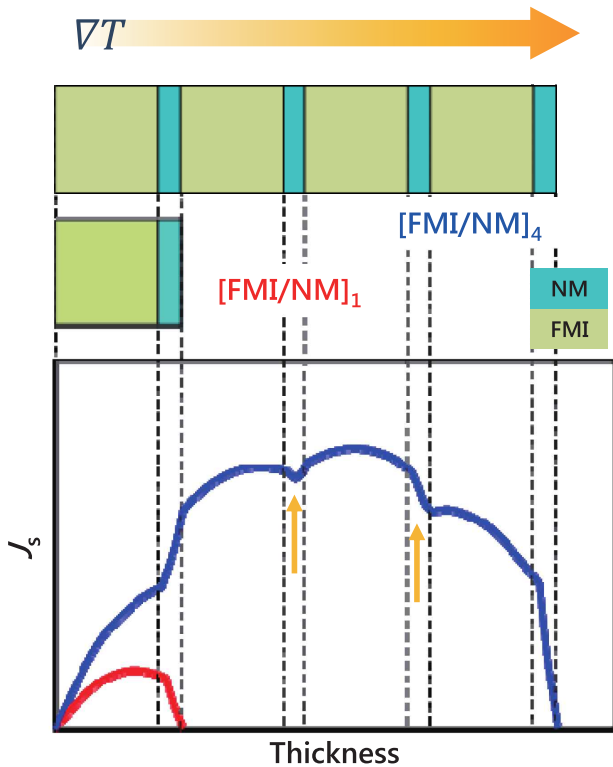


Figure 1 A example of the spin current profile calculated for  $[\text{FMI}/\text{NM}]_1$  and  $[\text{FMI}/\text{NM}]_4$  (FMI: ferromagnetic insulator, NM: nonmagnetic metal) (Ref. 3).

YIG: Ar 15 sccm, O<sub>2</sub> 0.3 sccm, RF150 W, and 11325 s

The deposition sequence for the normal-structured GGG/[YIG/Pt]<sub>n</sub>, the inverted-structured GGG/Pt/YIG, and GGG/Pt/YIG/Pt are as follows:

1. Annealing of the GGG substrates that face each other's polished sides, the so-called face-to-face configuration (F2F), at 900°C in air for 30 min. using an infrared lamp furnace (MILA5000).
2. Deposition of a 40-nm YIG film at room temperature using QAM-4.
3. Rapid thermal annealing (RTA) at 850°C for 200 seconds.
4. Deposition of a 5-nm Pt film at room temperature.
5. Deposition of a 40-nm YIG film on the Pt film, covered with an electrode area at both ends of the sample in order to ensure electrical conductivity with Pt.

Steps 3 through 5 were repeated to create a multilayered [YIG/Pt]<sub>n</sub> structure. The only difference in the GGG/Pt/YIG sample is a different deposition order for Pt and YIG.

## 2.2 Measurement method

Film thickness and crystallinity were checked with X-ray reflectometry (XRR) and X-ray diffraction (XRD), respectively. Detailed surface profiles were measured by AFM.

To evaluate the magnetic properties of the samples, we investigated both magnetization and ferromagnetic resonance (FMR). In ferromagnetic materials, spin waves are excited by microwave irradiation of the material in a magnetic field. In the FMR experiments, the absorption of microwaves is measured while sweeping the magnetic field. The resonance frequency can be expressed as  $2\pi f = \gamma H$  (where  $\gamma$  is a gyromagnetic ratio), and strong absorption is exhibited when the microwave frequency matches the resonance frequency. The width of the absorption spectrum obtained by sweeping the magnetic field is correlated to the attenuation of the spin wave: the smaller the spin wave attenuation, the narrower the line width. For well-studied materials such as YIG, this method is used for evaluating the quality of the samples. Because the SSE voltage is generated by the spin

current due to magnon diffusion driven by temperature differences, the line width in the FMR spectrum has become an important index.

For the SSE measurements, we used the sample holder made of AlN shown in Figure 2. The sample was sandwiched between the top and bottom AlN plates. The sample was cut to a size of 8 mm × 2 mm to adjust the holder. The length of the YIG layer touching the top plate is 5–6 mm. The Peltier element is held between the bottom AlN plate and a stage made of oxygen-free copper, which acts as a hot bath. The sample can be heated or cooled depending on the magnitude and direction of the electrical current applied to the Peltier element. The top AlN plate is connected to the Cu stage via a Mo screw with high thermal conductivity, so that heat can quickly escape to the hot bath. This serves to create a temperature gradient perpendicular to the film. The holder is positioned between the magnetic cores of the electromagnets and a magnetic field is applied along the short side of the sample. Then, the SSE voltage generated along the long side of the sample is measured. The electric field  $E$  created by SSE can be expressed as follows using temperature gradient  $\Delta T$  and magnetization  $M$ :

$$E = S \left( \frac{M}{|M|} \times \Delta T \right)$$

$S$  denotes the spin Seebeck coefficient (SSE coefficient). Using sample length  $L_{sample}$  and thickness  $D_{sample}$ , as well as the SSE voltage  $V_{SSE}$  and temperature gradient  $\Delta T$ ,  $S$  can be estimated as follows:

$$S = \frac{V_{SSE}/L_{sample}}{\Delta T/D_{sample}}$$

## 3. Experiment results and discussion

### 3.1 Structure of multilayered films

Figure 3(a) shows the AFM image of the GGG (110) substrate after the heat treatment at 900°C. The heat treatment caused a step & terrace (S&T) structure to appear on the GGG surface. The root mean square (RMS) roughness of the GGG substrate was 0.13 nm.

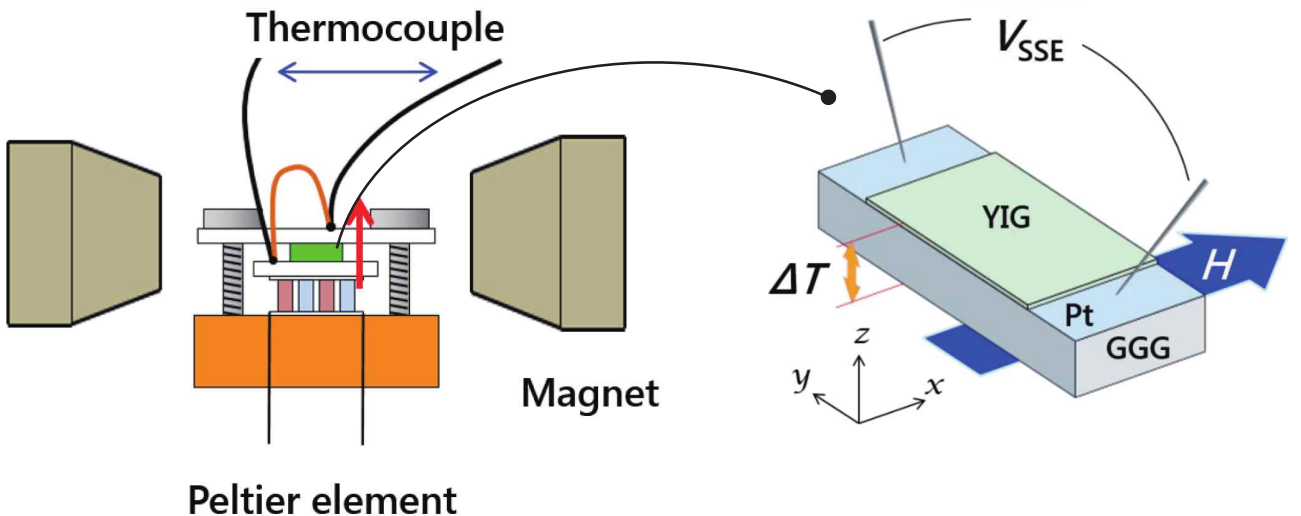


Figure 2 Schematic diagrams of the equipment for the measurement of the spin Seebeck effect (SSE) and the directions of the external field, the temperature gradient, and the SSE voltage.

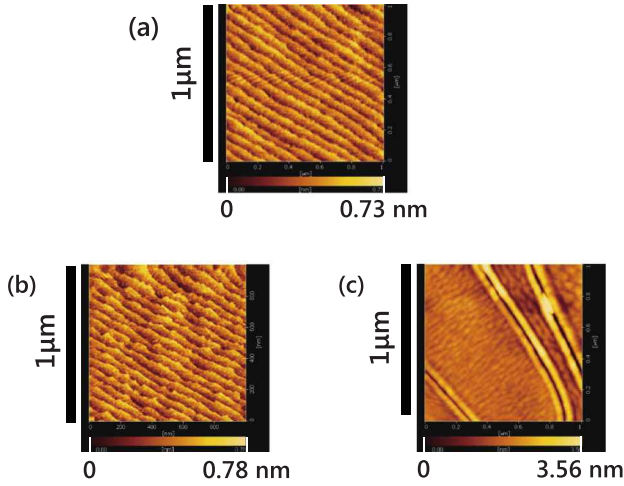


Figure 3 AFM images of (a) GGG (110) substrate after annealing at 900°C, (b) YIG film deposited on GGG substrate after RTA at 825°C and (c) YIG film deposited on GGG/Pt(5 nm) after RTA at 825°C.

Figures 3(b) and (c) show the AFM images of the surfaces of GGG/YIG and GGG/Pt/YIG after RTA. On GGG/YIG, S&T with the same cycle and orientation as that seen on the surface of the GGG substrate was observed. In addition, the RMS was 0.10 nm, which was essentially the same as on the GGG substrate, implying that the YIG film has high crystallinity. Meanwhile, S&T was not observed on GGG/Pt/YIG; instead, large cracks had occurred. Because of this, RMS roughness was 0.52 nm, which was four times that of the GGG substrate. Additionally, one-directional stratified structures were observed in the flat area, indicating that the film has crystalline domains with orientations different from the GGG substrate.

XRR measurements of GGG/YIG/Pt and GGG/Pt/YIG after YIG film deposition and RTA indicated that the film thickness of Pt and YIG is 5.2 nm and 48 nm, respectively, and roughness is around 0.2 nm.

According to XRD measurements of GGG/YIG around GGG (880) between 88° and 91°, a weak (880) peak of YIG was observed on the lower-angle side of the sharp (880) peak of GGG, indicating crystallization of YIG. The lattice constant in the direction perpendicular to the film was 1.248 nm, which is greater than the reported lattice constant of 1.2376 nm for the YIG bulk. This is the same as in the previous literature, and is considered to be the lattice expansion effect of the thin film compared with the bulk crystal<sup>(4)-10)</sup>.

As for GGG/Pt/YIG, XRD measurements were performed over a wide range from 31° to 91°. However, no peak belonging to YIG was observed, even though the AFM results seemed to imply that YIG had become polycrystalline. We concluded that the YIG film was so thin that the XRD equipment was not sensitive enough to obtain the intensity of the diffraction.

On the lower-angle side of GGG (440) and (880), broad peaks of Pt (111) and (222) were also observed. Laue oscillations were also clearly observed, which shows that the

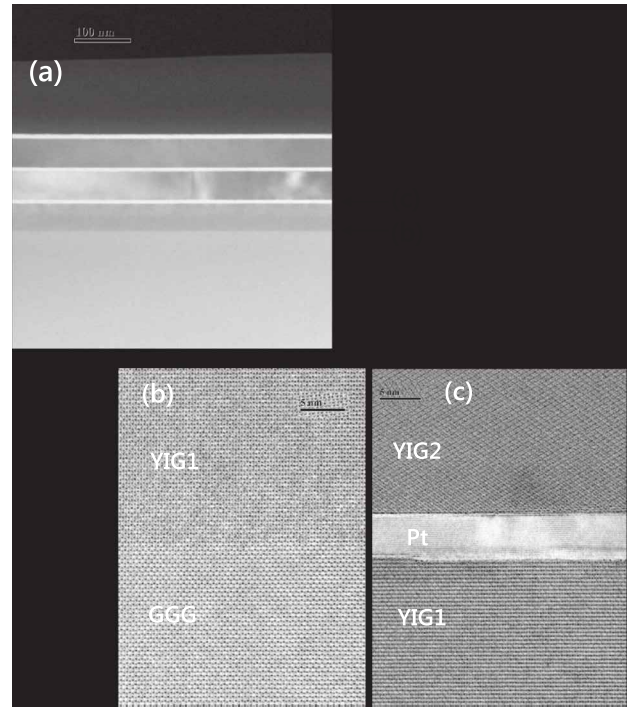


Figure 4 TEM images of GGG/[YIG(48 nm)/Pt(5.2 nm)]<sub>3</sub>. (a) A low magnification image of the substrate and all layers, (b), (c) high magnification images of the interfaces indicated at arrows in (a).

Pt layer is extremely flat. In addition, no peak belonging to Pt (200) appeared, and the RTA had caused the Pt layer to crystallize so as to form a (111) plane parallel to the film.

Figure 4(a) shows a cross-sectional TEM image of multilayered GGG/[YIG/Pt]<sub>3</sub>, and (b) is a high-magnification image of the interface between the GGG substrate and the first YIG layer, showing that YIG is continuously linked to GGG and has grown epitaxially without any defects. In contrast, in the high-magnification image of the interface between the first and second YIG layer across the Pt layer shown in (c) in Figure 4, the second YIG layer has a different crystal orientation from the first YIG layer. From (a) in Figure 4, it can be seen that the second and third YIG layers have become polycrystalline on the Pt layers. Polycrystallization of YIG can also be confirmed in the cross-sectional TEM image of GGG/Pt/YIG, and it was found that the cracks observed in the AFM images were polycrystalline grain boundaries. Although the interior of the grains surrounded by cracks consists of microscopic single-crystals, the film as a whole is polycrystalline. In most cases, the film thickness direction is taken up by a single microcrystal.

To evaluate the magnetism of the fabricated YIG, its FMR was measured. Before RTA, no resonance absorption peak of FMR was observed. This is because YIG is amorphous in the as-deposited state and does not exhibit magnetism. Figure 5 shows the FMR spectra of GGG/YIG/Pt and GGG/Pt/YIG. The graph shows the derivative of the FMR absorption line, and the difference between the magnetic fields at which the curve indicates the maximum and minimum values is treated as the FMR line width. In the FMR spectrum of GGG/YIG/Pt, sharp absorption appeared at 2330 Oe and the line width was 4.1 Oe. This is roughly

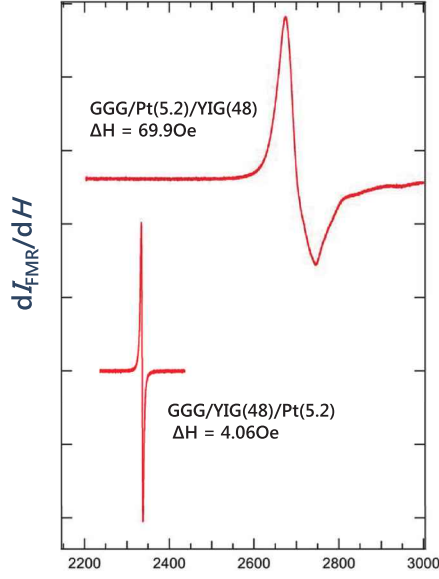


Figure 5 FMR spectra of GGG/Pt (5.2 nm)/YIG (48 nm) and GGG/YIG (48 nm)/Pt (5.2 nm).

the same as the FMR line width reported on YIG films epitaxially grown using the pulse laser deposition or sputtering method<sup>9-10</sup>).

On the other hand, in the FMR spectrum of GGG/Pt/YIG, a broad absorption peak appeared over the range between 2500 and 3000 Oe. The line width was 70 Oe. In magnetic materials exhibiting anisotropy, the locations at which FMR absorption occurs in the magnetic fields differ depending on the direction of the applied field. Because YIG also has magnetic anisotropy, in polycrystalline GGG/Pt/YIG, the absorption by YIG microcrystals with random orientations is distributed widely, and the scattering of spin waves at the crystal grain boundaries causes the spin waves to attenuate. These factors are considered to broaden the absorption peak.

Based on the above results, it can be understood that an RTA process causes as-deposited amorphous YIG to crystallize through solid-phase epitaxy using GGG as the seed crystal. However, in GGG/Pt/YIG, GGG could not be used as the seed because of the presence of the Pt layer, and random YIG crystal nuclei occurred everywhere in the film, making it become a polycrystalline film with boundaries.

### 3.2 Dependence of SSE on YIG film thickness

To investigate the diffusion of spin current within YIG, we examined the film-thickness dependence of SSE on YIG film thickness. As explained with regard to  $\text{Fe}_3\text{O}_4$  in Sec-

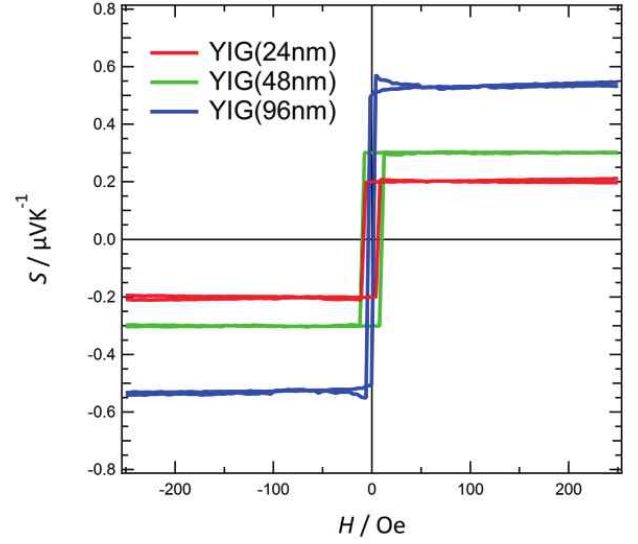


Figure 6 Field dependence of SSE coefficients of GGG/YIG (d)/Pt (4.2 nm),  $d = 24, 48$  and  $96$  nm, measured under the temperature difference condition of  $\Delta T = 6$  K.

tion 1, because the spin current within a magnetic material increases until the film thickness roughly matches the spin current diffusion length, the SSE also increases with the film thickness.

Changes in the SSE voltage relative to the YIG film thickness have been investigated in the past, and in YIG film fabricated using liquid phase epitaxy (LPE), the SSE voltage increases along with the film thickness of up to  $10\text{--}100 \mu\text{m}$ <sup>11</sup>). Because the SSE is generated by the spin current within the distance of the magnon diffusion length from the YIG-Pt interface, the film thickness at which SSE becomes saturated is roughly the same as the magnon diffusion length of YIG. In the film synthesized by LPE, the magnon diffusion length was  $1 \mu\text{m}$  or longer, but in the film deposited by sputtering, the length could not be clearly determined.

Table 1 summarizes the magnetization of GGG/YIG(d)/Pt (4.2) and the FMR spectrum line width for YIG with varying film thicknesses ( $d = 24, 48$ , or  $96$  nm). The magnitude of magnetization is constant and there are no differences in the magnetic characteristics. The magnon diffusion length is inversely proportional to the magnitude of spin wave attenuation. The FMR line width is constant among the three film thickness samples, which are suitable for estimating the magnon diffusion length from the SSE.

Table 1 Resistivities of Pt layers, the magnetizations and the FMR line widths of GGG/YIG (d)/Pt(4.2 nm),  $d = 24, 48$  and  $96$  nm.

|           | Resistivity<br>$\mu\Omega\text{cm}$ | Magnetization<br>$\text{emu cm}^{-3}$ | FMR line<br>width<br>Oe |
|-----------|-------------------------------------|---------------------------------------|-------------------------|
| YIG 24 nm | 20.13                               | 106                                   | 5.5                     |
| YIG 48 nm | 20.83                               | 101                                   | 4.3                     |
| YIG 96 nm | 19.61                               | 102                                   | 6.3                     |

Table 2 Resistivities of Pt layers of GGG/[YIG (48 nm)/Pt (5.2 nm)]<sub>n</sub> ( $n = 1, 2$  and  $3$ ), GGG/Pt (5.2 nm)/YIG (48 nm) and GGG/Pt (5.2 nm)/YIG (48 nm)/Pt (5.2 nm).

| GGG/[YIG (48)/Pt (5.2)] <sub>n</sub> | Resistivity $\mu\Omega\text{cm}$ |
|--------------------------------------|----------------------------------|
| $n=1$                                | 17.5                             |
| $n=2$                                | 18.3                             |
| $n=3$                                | 18.5                             |
|                                      |                                  |
| GGG/Pt (5.2)/YIG (48)                | 17.5                             |
| GGG/Pt (5.2)/YIG (48)/Pt (5.2)       | 18.6                             |

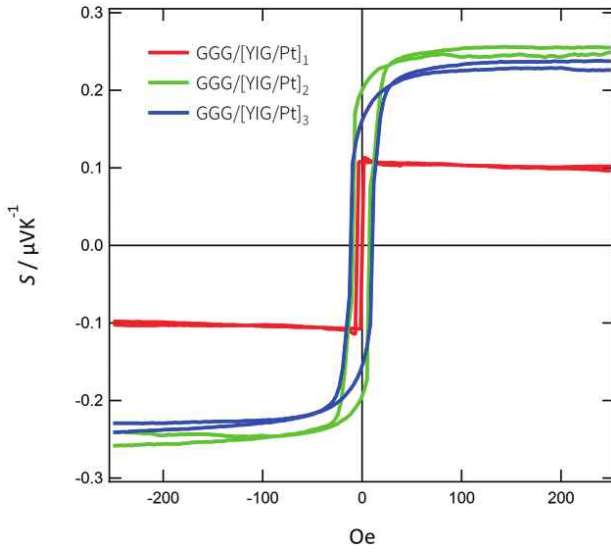


Figure 7 Field dependence of SSE coefficients of GGG/[YIG (48 nm)/Pt (5.2 nm)]<sub>n</sub>,  $n = 1-3$ , measured under the temperature difference condition of  $\Delta T = 6$  K.

Figure 6 shows the field dependence of the SSE coefficient  $S$  measured at the temperature difference  $\Delta T$  of 6K. The saturation value of  $S$  at 200 Oe was  $0.2 \mu\text{VK}^{-1}$  at a film thickness of 24 nm, but increased to  $0.54 \mu\text{VK}^{-1}$  as the film thickness increased to 96 nm. The figure shows that the diffusion length of the spin current in the sputtering-deposited YIG film is 100 nm or longer.

### 3.3 SSE of multilayered GGG/[YIG/Pt]<sub>n</sub>

Table 2 shows the resistivity of Pt. The resistivity remains constant even when the number of layers increases. Figure 7 shows the field dependence of the SSE coefficient  $S$  of GGG/[YIG(48)/Pt(5.2)]<sub>n</sub> ( $n = 1-3$ ) measured when the temperature difference  $\Delta T$  was 6 K. The  $S$  value at 200 Oe was determined as the saturation value.

At  $n = 1$ , the  $S$  value was  $0.1 \mu\text{VK}^{-1}$ , but it roughly doubled to  $0.23 \mu\text{VK}^{-1}$  at  $n = 2$ . However, when the number of layers was increased from two to three ( $n = 3$ ), the SSE hardly changed, as indicated by the  $S$  value of  $0.24 \mu\text{VK}^{-1}$  at  $n = 3$ .

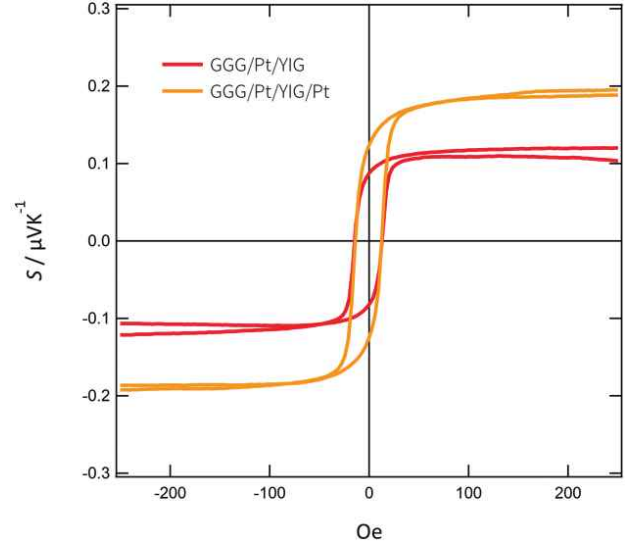


Figure 8 Field dependence of SSE coefficients of GGG/Pt (5.2 nm)/YIG (48 nm)/Pt (5.2 nm) and GGG/Pt (5.2 nm)/YIG (48 nm), measured under the temperature difference condition of  $\Delta T = 6$  K.

From the SSE coefficient  $S$  and the sheet resistance  $R_s$ , the output per unit area of element (SSE output characteristic) can be estimated as  $S^2/R_s$ . Although the SSE coefficient doubled from  $n = 1$  to  $3$ , the SSE output characteristic increased by 16 times because the sheet resistance decreased as the number of layers increased due to the constant resistivity of Pt.

In  $[\text{Fe}_3\text{O}_4/\text{Pt}]_n$  introduced in Section 1.2,  $S$  continued to increase up to  $n = 6$ , which is different from the result for  $[\text{YIG}/\text{Pt}]_n$ . In the samples where  $n = 2$  or  $3$ , the YIG layers sandwich the Pt layer from the top and bottom, such as YIG/Pt/YIG. In a simplified model, because of the contribution to the spin current from the two Pt-YIG interfaces on the top and bottom, the SSE voltage increases by 2 times. Taking the enhancement and circuit made by the multilayers into account, the SSE voltage of multilayered GGG/[YIG/Pt]<sub>n</sub> increases by  $(2n-1)/n$  times (where  $n$  denotes the number of layers) and gradually approaches twice the original size. Because SSE nearly doubled when  $n = 2$  in the results obtained in our study, this simple interpretation does not suffice. Therefore, we investigated the effects of increases in the number of YIG/Pt interfaces on SSE.

### 3.4 SSE of GGG/Pt/YIG and GGG/Pt/YIG/Pt

Next, we measured the SSE of GGG/Pt/YIG and GGG/Pt/YIG/Pt, with the latter sample having an additional Pt layer. Figure 8 shows the field dependence of the SSE coefficient  $S$  of GGG/Pt/YIG and GGG/Pt/YIG/Pt. The saturation value of  $S$  at 200 Oe was  $0.11 \mu\text{VK}^{-1}$  for GGG/Pt/YIG. This value is nearly equal to that for GGG/YIG/Pt. As discussed in Section 3.1, the FMR line width on GGG/Pt/YIG is 70 Oe, which is more than 10 times greater than the FMR line width on GGG/YIG, which is 4.1 Oe. This is because the YIG on top of the Pt is polycrystalline and the attenuation of its spin wave is large. However, a correlation between the spin current attenuation and the magnitude of the SSE

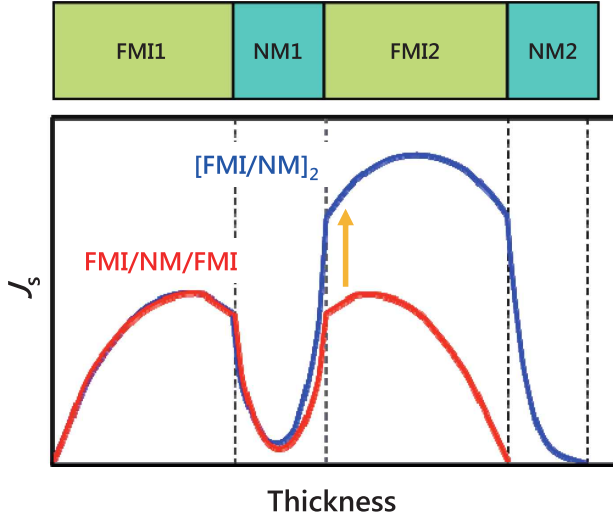


Figure 9 Comparison of the spin current profile for the SSE models,  $[FMI/NM]_2$  and FMI/NM/FMI (FMI: ferromagnetic insulator, NM: nonmagnetic metal) (Ref. 3). At the interface between NM1 and FMI2, the spin current is enhanced for  $[FMI/NM]_2$ .

voltage was reported – the larger the attenuation rate, the smaller the SSE voltage<sup>12</sup>). Although our results seem to contradict these findings at first glance, it must be noted that the comparison made in Reference 12 was between single-crystalline YIG film samples. The relationship between the SSE voltage and the spin wave attenuation propagated from the single-crystalline film to the polycrystalline film is not clear. As shown in Section 3.1, the YIG film of GGG/Pt/YIG is a polycrystalline film, but the film thickness is taken up by only a single grain, which does not prevent the diffusion of spin current in the film thickness direction, and therefore its effect on the SSE voltage is also considered small.

The SSE coefficient  $S$  of GGG/Pt/YIG/Pt was  $0.19 \mu\text{VK}^{-1}$ , which was 173% greater than that of GGG/Pt/YIG. The interpretation about YIG/Pt/YIG explained in the previous section does not apply at all to this structure. Therefore, we think that the mechanism of enhancement of the spin current is at work behind this increase in the same way as in  $[\text{Fe}_3\text{O}_4/\text{Pt}]_n$ , described in the Introduction. The thermal resistance achieved by stacking Pt is not large enough to increase the temperature difference, because the thickness of Pt is only 5 nm and it is an excellent conductor. In Reference 3, Ramos, et al., calculated the distribution of spin current in the film thickness direction in a stacked structure consisting of a nonmagnetic metal (NM) and a ferromagnetic insulator (FMI) (Figure 9). It has been reported that adding an NM layer on top of FMI/NM/FMI, thereby obtaining an FMI/NM/FMI/NM structure, increases the spin current at the NM/FMI interface indicated by the arrow in Figure 9. We think that the increase in the SSE in GGG/Pt/YIG/Pt in our experiments can be explained by this effect. However, in the study cited in Reference 3, the SSE voltage increased in mul-

tilayered  $[\text{Fe}_3\text{O}_4/\text{Pt}]_n$  up to  $n=6$ , and therefore their theory cannot be applied to the results we obtained on  $[\text{YIG}/\text{Pt}]_n$ . Further investigation is needed.

#### 4. Conclusion

In this study, we fabricated an epitaxial YIG crystal film on GGG, and further, a GGG/Pt/YIG structure by placing a Pt layer between them. Although the YIG on the Pt layer is polycrystalline, the intensity of the SSE coefficient was almost equal to that of GGG/YIG/Pt in which YIG is single-crystalline. In multilayered GGG/ $[\text{YIG}/\text{Pt}]_n$ , although the SSE nearly doubled when  $n=1$ , the resistivity of Pt remained constant and the output characteristic improved by 16 times when the number of layers increased. Meanwhile, we confirmed that the SSE increased in the sandwich structure of Pt/YIG/Pt as well, which is considered to be due to the effect of the spin current enhanced partially by the multilayered structure, described in Reference 12, has partially materialized. Although the SSE coefficient is still extremely small, on the order of  $\mu\text{VK}^{-1}$ , we were able to use sputtering and RTA to fabricate high-quality multilayered structures that showed increases in the SSE coefficient and improvements in the output characteristics.

Our study was conducted jointly with the Saitoh Laboratory at the AIMR, Tohoku University. We would like to express our sincere appreciation to Assistant Professor Yoshikawa and Professor Saitoh, who guided our experiments.

#### References

- 1) A. Kirihara, et al., *Sci. Rep.* **6** (2016), 23114.
- 2) K. Uchida, et al., *Proceedings of the IEEE* **104** (2016), 1499.
- 3) R. Ramos, et al., *Phys. Rev. B* **92** (2015), 220407.
- 4) C. Tang, et al., *Appl. Phys. Lett.* **108** (2016), 102403.
- 5) C. Hauser, et al., *Sci. Rep.* **6** (2016), 20827.
- 6) Y. Sun, et al., *Appl. Phys. Lett.* **101** (2012), 152405.
- 7) T. Liu, et al., *J. Appl. Phys.* **115** (2014), 17A501.
- 8) M. C. Onbasli, et al., *APL Materials* **2** (2014), 106102.
- 9) O. d'Allivy Kelly, et al., *Appl. Phys. Lett.* **103** (2013), 082408.
- 10) J. Lustikova, et al., *J. Appl. Phys.* **116** (2014), 153902.
- 11) E. J. Gao, et al., *Phys. Rev. X* **6** (2016), 031012.
- 12) H. Chang, et al., *Sci. Adv.* **3** (2017) e1601614.